



Ascorbic acid-assisted solvothermal synthesis of $\text{LiMn}_{0.9}\text{Fe}_{0.1}\text{PO}_4/\text{C}$ nanoplatelets with enhanced electrochemical performance for lithium ion batteries

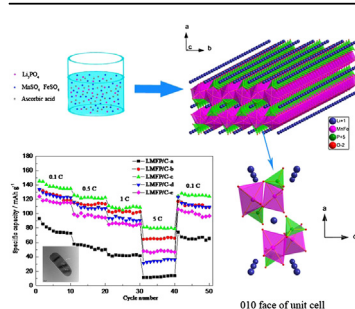
Pengjian Zuo*, Guangyu Cheng, Liguang Wang, Yulin Ma, Chunyu Du, Xinqun Cheng, Zhenbo Wang, Geping Yin

Institute of Advanced Chemical Power Source, School of Chemical Engineering and Technology, Harbin Institute of Technology, Harbin 150001, China

HIGHLIGHTS

- LMFP/C powders were prepared by an ascorbic acid-assisted solvothermal process.
- The LMFP/C sample exhibits an excellent discharge capacity of 145 mA h g^{-1} .
- The LMFP/C holds highly uniform distribution of particle size and better conductivity.

GRAPHICAL ABSTRACT



ARTICLE INFO

Article history:

Received 30 April 2013

Received in revised form

17 June 2013

Accepted 17 June 2013

Available online 26 June 2013

Keywords:

Lithium manganese phosphate

Nanoplatelet structure

Ascorbic acid-assisted solvothermal

synthesis

Lithium ion battery

ABSTRACT

Morphology-controlled $\text{LiMn}_{0.9}\text{Fe}_{0.1}\text{PO}_4$ nanoplatelets as high performance cathode material for lithium ion batteries have been synthesized *via* a simple ascorbic acid-assisted solvothermal process in water-ethanol solvent. The phase structure and morphology of the products were characterized by XRD, SEM and TEM. The results reveal that decreasing the crystallite size along *b*-axis direction and increasing the surface area of (010) plane can shorten Li^+ diffusion path and increase the electrode reaction activity. The $\text{LiMn}_{0.9}\text{Fe}_{0.1}\text{PO}_4$ nanoplatelet holds the high capacity of 145 mA h g^{-1} , 134 mA h g^{-1} , 119 mA h g^{-1} , 97 mA h g^{-1} and 68 mA h g^{-1} at 0.1 C, 0.5 C, 1 C, 5 C and 10 C respectively, and it can retain 75% of the initial reversible capacity even after 100 cycles at 10 C rate.

© 2013 Elsevier B.V. All rights reserved.

1. Introduction

Olivine-structured lithium transition-metal phosphates (LiMPO_4 , M = Mn, Fe, Co, Ni) are attractive cathode materials for rechargeable lithium ion batteries because of their low cost,

environmental benignity, and thermal stability originated from strong P–O bonds [1,2]. Among them, many research efforts have focused on LiFePO_4 (LFP) because of its excellent cycling stability and remarkable rate capability obtained by particle size minimization, carbon coating and cation doping [3–9]. However, the low operating potential of LFP (3.4 V vs. Li^+/Li) indicates a low energy density which limits its application for hybrid electric vehicles (HEVs) and plug-in HEVs (PHEVs). The successful commercialization of LFP has stimulated the development of olivine LiMnPO_4 (LMP). LiMnPO_4 is

* Corresponding author. Tel./fax: +86 451 86403216.

E-mail addresses: zuopj@hit.edu.cn, zuopjhit@gmail.com (P. Zuo).

more promising in comparison with LFP in terms of its high energy density induced by the working voltage (4.1 V vs. Li^+/Li) and the similar theoretical capacity of 170 mA h g^{-1} . However, the commercial application of LiMnPO_4 still faces a great challenge, which is related to the poor Li^+ insertion/de-insertion kinetics caused by the Jahn–Teller lattice deformation and structural changes of LiMnPO_4 during cycling [10–12]. In order to prepare the high performance of LiMnPO_4 , several approaches have been attempted, such as the solid-state reaction [13,14], sol–gel method [15,16], polyol process [6,17,18], hydrothermal synthesis [14,19], solvothermal method [20–23], precipitation [24,25], and the electrostatic spray deposition [26]. The solvothermal reaction is an effective method to obtain nanostructured materials with well-defined morphology [26–28]. Since lithium ion diffusion in the olivine structured LiMnPO_4 is anisotropic, morphology control is of significant importance to improve the electrochemical performance of LiMnPO_4 besides size miniaturization [21].

Recent theoretical computational results on LiMnPO_4 have shown that, in the orthorhombic olivine structure, lithium ion diffusion in the lattice is uniaxial along the *b*-direction, where Li ions hop between octahedral sites via a tetrahedral hole formed by the edge-sharing LiO_6 octahedra [29–31]. If the LiMnPO_4 nanocrystal grows with a short length perpendicular to the *b*-direction, the rate capability of the batteries employing LiMnPO_4 nanoplates as cathode materials could be improved significantly. Mono-dispersed LiMnPO_4 nanocrystals for Li ion batteries have been prepared successfully by a solvothermal method in a mixed solvent of water and polyethylene glycol (PEG) [21]. The LMP nanoplate/graphene composites delivered a capacity of 149 mA h g^{-1} at 0.1 C and 64 mA h g^{-1} at 5 C with an excellent cycling stability. N.H. Kwon et al. [23] reported the synthesis of LiMnPO_4 nanoparticles with 5–10 nm thin rod by an improved thermal decomposition method, and the LiMnPO_4 electrode provided a discharge capacity of 165 mA h g^{-1} at 1/40 C and 66 mA h g^{-1} at 1 C with 10 wt% carbon addition.

Several literature on LiMnPO_4 have shown that the partial substitution of Mn with other bivalent metal cations such as Mg, Fe, Ni and Zn can enhance the electrochemical reaction capability of $\text{Mn}^{2+}/\text{Mn}^{3+}$ redox couple in LiMnPO_4 [14,32,33]. Molenda et al. [34,35] reported that the electrical conductivity of $\text{LiFe}_{0.45}\text{Mn}_{0.55}\text{PO}_4$ is one order of magnitude higher than that of the un-doped LFP. A recent result reported by K. Saravanan et al. [8] showed that the lower activation energy of electronic conductivity for the iron–manganese solid solution maximizes the manganese utilization with a superior rate storage performance in comparison with LiMnPO_4 . However, the electrochemical performances of LiMnPO_4 with Fe^{2+} substitution are not satisfactory so far even though many efforts have been made in terms of the improvement of electronic conductivity [34–38].

In this paper, through using ascorbic acid ($\text{C}_6\text{H}_8\text{O}_6$) as reducing agent and morphology control agent, a facile solvothermal synthesis method of $\text{LiMn}_{0.9}\text{Fe}_{0.1}\text{PO}_4$ (LMFP) nanoplatelets in a mixed solvent containing water and ethanol was proposed. Structure and morphology analysis as well as electrochemical performance were performed systematically by XRD, SEM, FTIR, EIS and charge–discharge tests, and the effects of ascorbic acid on structure, morphology and electrochemical properties of LMFP/C nanoplatelets were also investigated in detail.

2. Experimental

2.1. Synthesis

The materials were prepared by the solvothermal method in water–ethanol solvent. The detailed procedures are as follows:

LiOH , H_3PO_4 , MnSO_4 and FeSO_4 with a molar ratio of 3:1:0.9:0.1 were dissolved in 60 ml ethanol–water (1:1 by volume) solvent under stirring, and then a series of ascorbic acids of 0 g (i.e. without ascorbic acid for the purpose of comparison), 0.4 g, 0.8 g, 1.2 g, and 1.6 g were added to prepare the LMFP products which were denoted as LMFP-a, LMFP-b, LMFP-c, LMFP-d, and LMFP-e, respectively. The pH value of the suspension was controlled in the range of 5.5–6.0 by H_3PO_4 . After 6 h vigorous stirring, the suspension was transferred into a 100 ml Teflon-lined stainless steel autoclave followed by a solvothermal treatment at 200°C for 15 h. The obtained gray precipitate was filtered, washed several times with ethanol and distilled water, and dried in the vacuum oven at 80°C for 5 h. For the LMFP/C synthesis, glucose and LMFP powders with a weight ratio of 1:2 were blended using a high-energy ball-milling machine (Fritsch pulverisette 7) at 350 rpm for 5 h, then the mixture was dried and ground. The as-prepared powders were annealed in a tubular furnace at 300°C for 3 h, and then heated at 600°C for 5 h in Ar/H_2 atmosphere ($\text{Ar}:\text{H}_2 = 95:5$) flow to obtain the carbon-coated LMFP samples denoted as LMFP/C-a, LMFP/C-b, LMFP/C-c, LMFP/C-d and LMFP/C-e, respectively.

2.2. Characterization

The crystalline phases of the samples were studied by X-ray powder diffraction (XRD, Rigaku D/max- γB) analyzer equipped with $\text{Cu K}\alpha$ radiation over the 2θ range of 10° – 90° . The morphology of the samples was observed by field-emission scanning electron microscope (FESEM, FEI Helios Nanolab600i) equipped with an Energy Dispersive Spectroscopy (EDS). The interior structure of the LMFP/C nanocomposites was observed by transmission electron microscopy (FETEM, FEI Tecnai G2 F30). Fourier transform infrared (FT-IR) spectra were recorded on thin transparent pellets of the dried sample and spectra pure KBr taken in 1:20 from 2000 to 400 cm^{-1} with 2 cm^{-1} resolution for 20 scans using a Thermo Scientific Nicolet iS10. To determine the actual amount of carbon in the LMFP/C nanocomposites, thermogravimetric analysis (TGA) was performed from room temperature to 650°C at a heating rate of $10^\circ\text{C min}^{-1}$ using the Netzsch STA449F3 in air atmosphere.

2.3. Electrochemical measurements

The electrochemical tests were carried out on a CR2025 coin cell. The cells were composed of a lithium metal negative electrode and a nanocomposite positive electrode that were separated by a microporous polypropylene film, and 1 mol l^{-1} solution of LiPF_6 in a mixed solvent of ethylene carbonate (EC) and dimethyl carbonate (DMC) with 1:1 in volume ratio was used as the electrolyte. The electrode was fabricated by mixing active material, acetylene black, and polyvinylidene fluoride (PVDF) binder dispersed in a *N*-methylpyrrolidone (NMP) solution in a weight ratio of 80:10:10. The capacities of the active materials are normalized by the weight of the $\text{LiMn}_{0.9}\text{Fe}_{0.1}\text{PO}_4$ in the electrodes. The resultant slurry was then coated on an aluminum foil and dried at 120°C for 10 h in a vacuum oven. The cells were assembled in a glove box filled with high-purity argon gas.

The electrochemical performance of the cells was examined using a battery testing system (Neware, BST-5V3mA) at different charge/discharge rates between 2.5 V and 4.6 V. The cells were charged at a CC-CP protocol, i.e., first charged at a constant current of 0.1 C–4.6 V followed by holding at 4.6 V until the current decaying to 0.02 C. For C-rate performance experiment, the cells were cycled with a constant charge rate of 0.1 C followed by the increasing discharge rates.

Measurements of electrochemical impedance spectroscopy and cyclic voltammetry were carried out using an electrochemical

analyzer (CHI604D). The amplitude of the AC signal was 5 mV in the frequency range from 100 kHz to 0.01 Hz. Cyclic voltammetry was performed between 2.5 V and 4.6 V at a scanning rate of 0.2 mV s⁻¹. All the electrochemical measurements were performed at room temperature.

3. Results and discussion

In the orthorhombic olivine structure of LMP, lithium ion transport follows a zigzag one-dimensional pathway along the *b* direction [39]. LMP nanocrystals show the identical orientation with preferred growth on the order of [010] > [001] > [100] with [010] and [001] being very close [4]. Therefore, LMP nanoplates with a face perpendicular to the [100] direction have a short length that is parallel to the *a*-axis, which is not electrochemically active for Li⁺ transport. In contrast, LMP nanoplatelets with (010) crystal planes possess the short length along the active *b*-axis for Li⁺ deintercalation/intercalation. If an LMP nanocrystal was to grow with a short length perpendicular to the [010] direction, the rate capability of the LMP nanocrystal will be improved significantly. Based on these considerations, we succeed in preparing Fe-doped LMP nanoplates with limited *b*-axis length by a solvothermal method and achieving the excellent electrochemical performance. Fig. 1 shows the schematic drawing of a solvothermal synthesis method of LMFP nanoplatelets and their crystallographic orientation.

The crystal structure of LMFP and carbon-coated LMFP was analyzed by X-ray powder diffraction. XRD patterns confirm the orthorhombic olivine structure with a *Pnma* space group and no detectable impurities in the samples synthesized by the solvothermal method (Fig. 2). The ascorbic acid as a reducing agent facilitates the formation of LMFP by providing a suitable reducing environment and suppressing the oxidation of Fe²⁺ and Mn²⁺. From Fig. 2b, the XRD patterns of the carbon-coated LMFP nanoplatelets do not show any additional peaks in comparison with LMP, indicating that the coated carbon may be in an amorphous phase. The calculated lattice parameters of LMFP and LMFP/C samples are listed in Table 1. It can be seen that the calculated lattice parameters and cell volume of the samples increase slightly after ball-milling followed by the heat treatment. It is also noticeable that the calculated lattice parameters of LMFP-c are *a* = 10.4132 Å, *b* = 6.0860 Å,

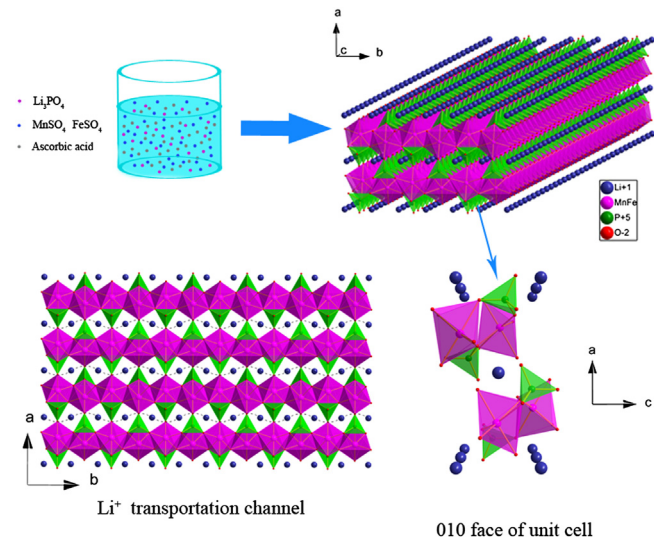


Fig. 1. Schematic illustration of solvothermal synthesis route and the crystallographic orientation of LMFP.

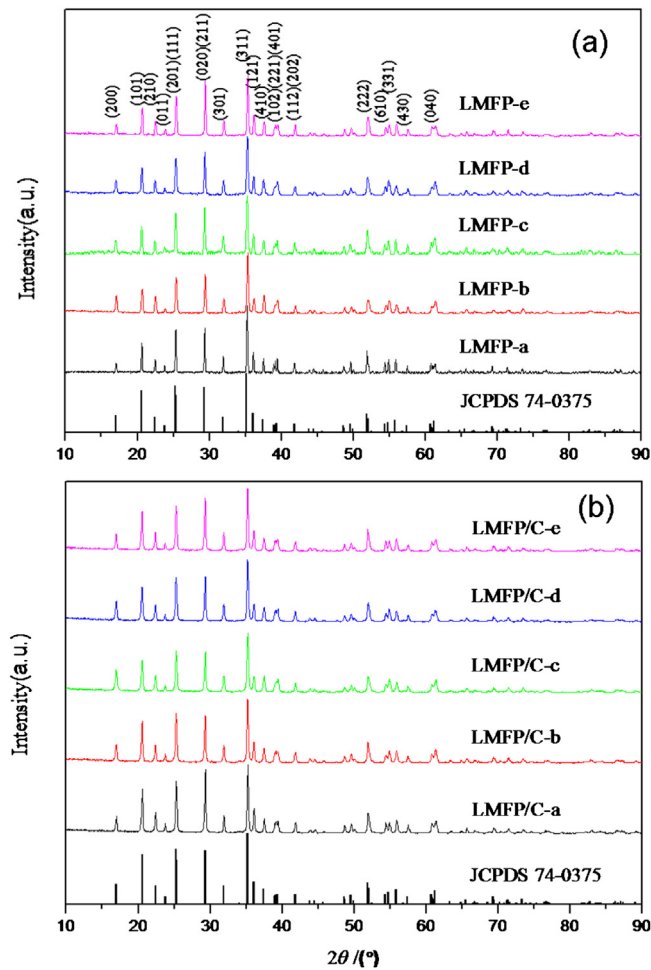


Fig. 2. XRD patterns of (a) LMFP and (b) LMFP/C samples.

c = 4.7284 Å, and *V* = 299.67 Å³, which reflects a compressed unit cell compared with that of the standard LMP (JCPDS no. 74-0375) of *a* = 10.46 Å, *b* = 6.1 Å, *c* = 4.744 Å, and *V* = 302.7 Å³. The decreasing unit cell volume of the Fe-doped composites in comparison with LMP is mainly associated with the smaller ionic radii of Fe²⁺ (0.92 Å) than that of Mn²⁺ (0.97 Å) [40].

The morphologies of pristine LMFP and carbon-coated LMFP were observed and the SEM images are shown in Fig. 3. LMFP synthesized by the solvothermal method shows a flakelike nanorod/nanoplate structure, and the size and the morphology of the products are dependent on the amount of ascorbic acid during the solvothermal synthesis process. The LMFP-c sample tends to be

Table 1
The calculated lattice parameters of LMFP and LMFP/C samples.

Samples	<i>a</i> (Å)	<i>b</i> (Å)	<i>c</i> (Å)	<i>V</i> (Å ³)
Standard LMP	10.46	6.1	4.744	302.7
LMFP-a	10.4239	6.0897	4.7342	300.53
LMFP-b	10.4154	6.0766	4.7217	298.85
LMFP-c	10.4132	6.0860	4.7284	299.67
LMFP-d	10.4254	6.0798	4.7329	300.0
LMFP-e	10.4064	6.0763	4.7312	299.17
LMFP/C-a	10.4220	6.0891	4.7361	300.56
LMFP/C-b	10.4298	6.0893	4.7382	300.93
LMFP/C-c	10.4284	6.0902	4.7374	300.89
LMFP/C-d	10.4283	6.0918	4.7356	300.84
LMFP/C-e	10.4318	6.0921	4.7385	301.15

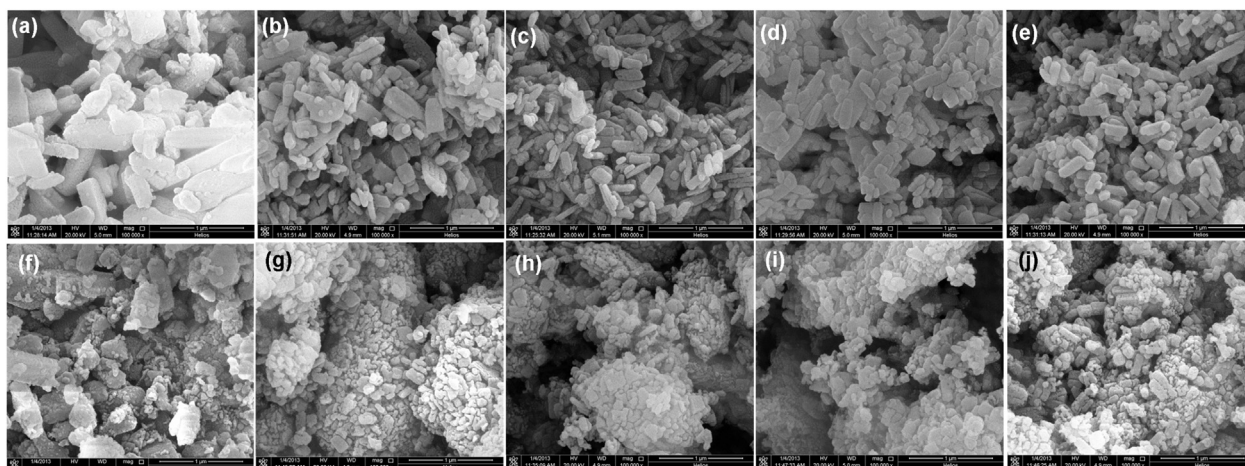


Fig. 3. SEM images of (a) LMFP-a; (b) LMFP-b; (c) LMFP-c; (d) LMFP-d; (e) LMFP-e; (f) LMFP/C-a; (g) LMFP/C-b; (h) LMFP/C-c; (i) LMFP/C-d and (j) LMFP/C-e.

smaller and more uniform flakelike nanorods with a size of *ca.* 40 nm in thickness, *ca.* 80 nm in width and less than 350 nm in length, which may be related to the decreased surface energy caused by the ascorbic acid molecule adsorption. Further, the formation of flakelike LMFP-c nanorods might be attributed to the strong effects between the ascorbic acid and precursors during the solvothermal process. Therefore, the ascorbic acid as reducing agent and morphology control agent plays a crucial role in the structure and morphology regulation during the solvothermal process. In order to enhance the electronic conductivity of the LMFP nanoplatelets, the LMFP samples were blended with glucose as carbon source by high-energy ball-milling followed by a heat treatment. It is worthy of noting that some large agglomerates are observed in the SEM images of LMFP/C samples, which are mainly due to the recombination between the LMFP nanoplatelets and the amorphous carbon obtained from the pyrolyzed glucose. The uniform element distribution can also be found in the element (C, Mn, Fe, P and O) mappings of LMFP/C-c sample (Fig. 4).

Transmission electron microscopy (TEM) was also carried out to confirm the microstructure of the LMFP-c and LMFP/C-c samples. It can be seen that the sample consists of well-separated flakelike nanorods as depicted in Fig. 5a and b. The neighboring lattice fringe distances of 3.057 Å and 3.752 Å correspond to the (020) and (011) crystal planes of LMFP, indicating the flakelike LMFP nanoplate's growth along the [001] direction with a limited thickness along *b* direction (Fig. 5c). For the LMFP nanoplatelets, the width along *b*-axis is in the range of 70–100 nm. As shown in the inset of Fig. 5d, some of the LMFP/C nanoplatelets are broken by the ball-milling process, which is unavoidable but beneficial to the enhancement of the electrochemical performance. LMFP nanoplatelets are coated and connected by carbon derived from the glucose, where the dark regions represent LMFP nanoplatelets and the light gray regions correspond to carbon. From the HR-TEM images shown in Fig. 5d, it is obvious that a uniform carbon coating with a thickness of ~ 3 nm exists on the surface of nanoplatelets. Hence, the electronic conductivity as well as the electrochemical performance of the LMFP material can be improved significantly.

The FTIR spectrum of LMFP/C-c in the 400–2000 wavenumber range corresponding to the stretching mode of PO_4^{3-} anion is shown in Fig. 6. The band at 982 cm^{-1} is assigned to the symmetric P–O stretching vibration, while the other three bands at 1074, 1106 and 1137 cm^{-1} are due to the asymmetric P–O stretching vibrations. The band near 634 cm^{-1} is ascribed to asymmetric bending mode, and the 582, 550, 499 and 456 cm^{-1} correspond to the bending modes of PO_4^{3-} [41]. The IR bands near 1625 cm^{-1} are attributed to

the symmetrical stretching of C=C [42]. Hence, FTIR results also confirm the presence of carbon in the carbon-coated $\text{LiMn}_{0.9}\text{Fe}_{0.1}\text{PO}_4$ nanoplatelets.

To confirm the carbon content of the LMFP/C nanoplatelets, thermogravimetric analysis of the samples was conducted in air, and the obtained TGA curves are shown in Fig. 7. The samples were heated from 30 to $650\text{ }^\circ\text{C}$ at a rate of $10\text{ }^\circ\text{C min}^{-1}$. The weight loss below $200\text{ }^\circ\text{C}$ is probably due to the evaporation of adsorbed moisture. It can be seen that the maximum weight loss of the

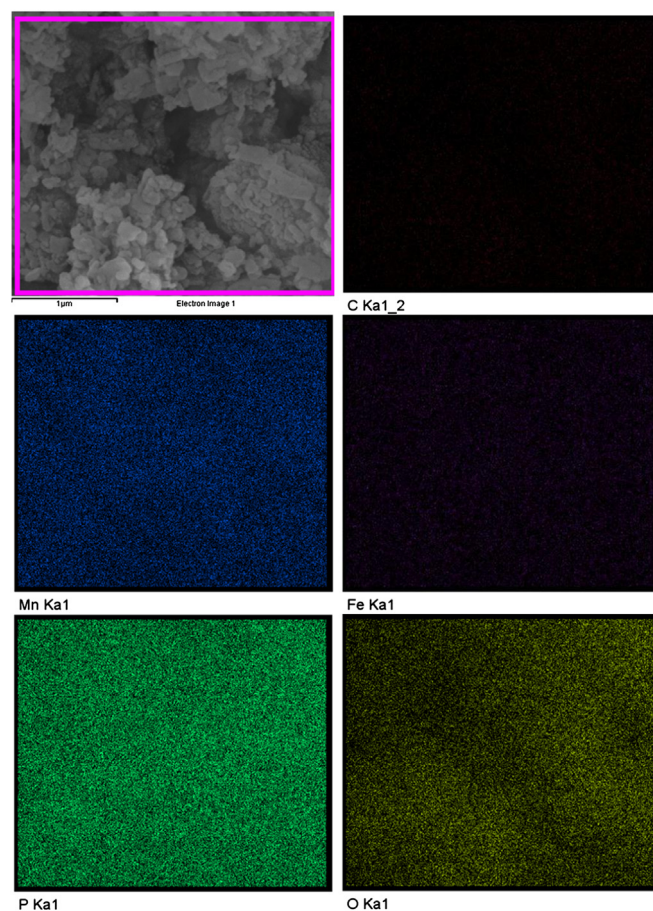


Fig. 4. Element mappings of LMFP/C-c.

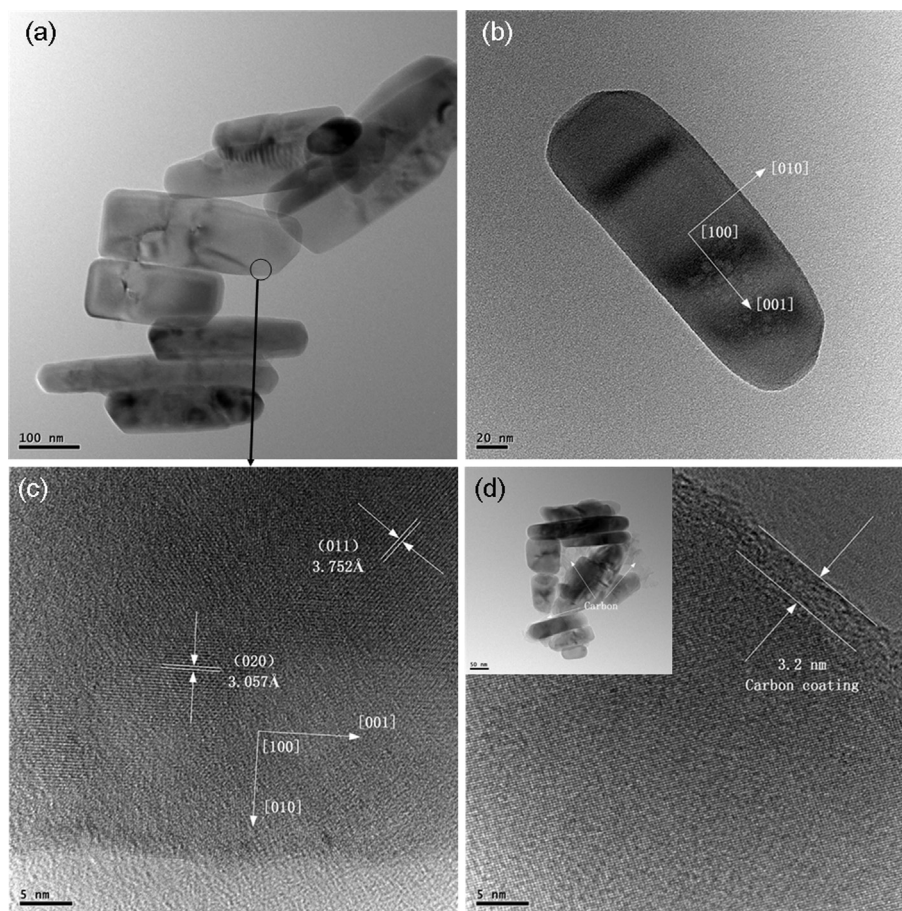


Fig. 5. (a, b) TEM images LMFP-c (c) HRTEM micrograph of the material and (d) HR-TEM micrograph of LMFP/C-c. SEM image of LMFP/C-c particles is also given as an inset.

samples located at 350–500 °C. The total carbon content is in the range of 10 wt%–12 wt%.

The charge/discharge experiments were used to evaluate the electrochemical performance of LMFP/C materials obtained by ascorbic acid-assisted solvothermal synthesis. The initial charge/discharge curves of LMFP/C nanosheet are shown in Fig. 8a–e. The voltage profiles clearly show a potential plateau around 4.1 V vs. Li^+/Li , indicating that the charge/discharge reaction proceeds via

a first-order phase transition between LiMnPO_4 and MnPO_4 [4]. In addition, the discharge voltage of the materials decreases markedly at the increasing discharge current, which can be mainly attributed to the large electrode polarization during the Li^+ diffusion process. As shown in Fig. 8a, the initial discharge capacity of LMFP/C-a drops to 34 mA h g^{-1} from 108 mA h g^{-1} when the current rate is increased to 5 C from 0.1 C. It can be seen from Fig. 8c that the LMFP/C-c nanosheets exhibit the highest specific capacity at the

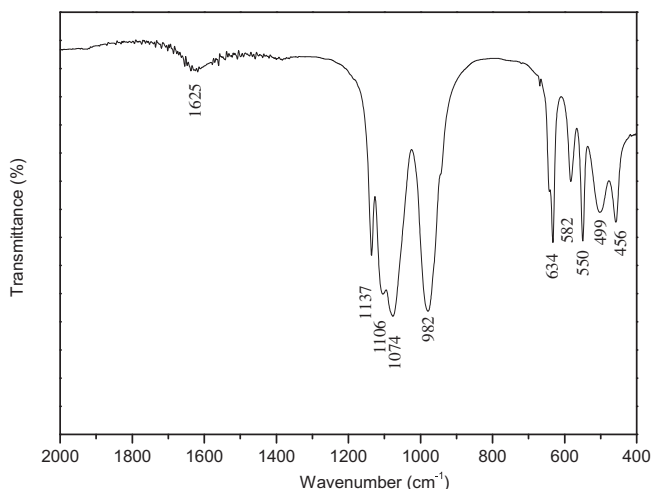


Fig. 6. FTIR spectra of LMFP/C-c sample.

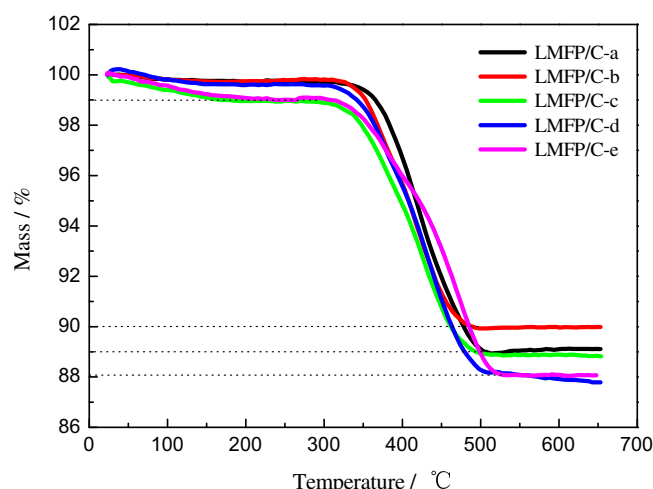


Fig. 7. TGA curves of LMFP/C at air atmosphere.

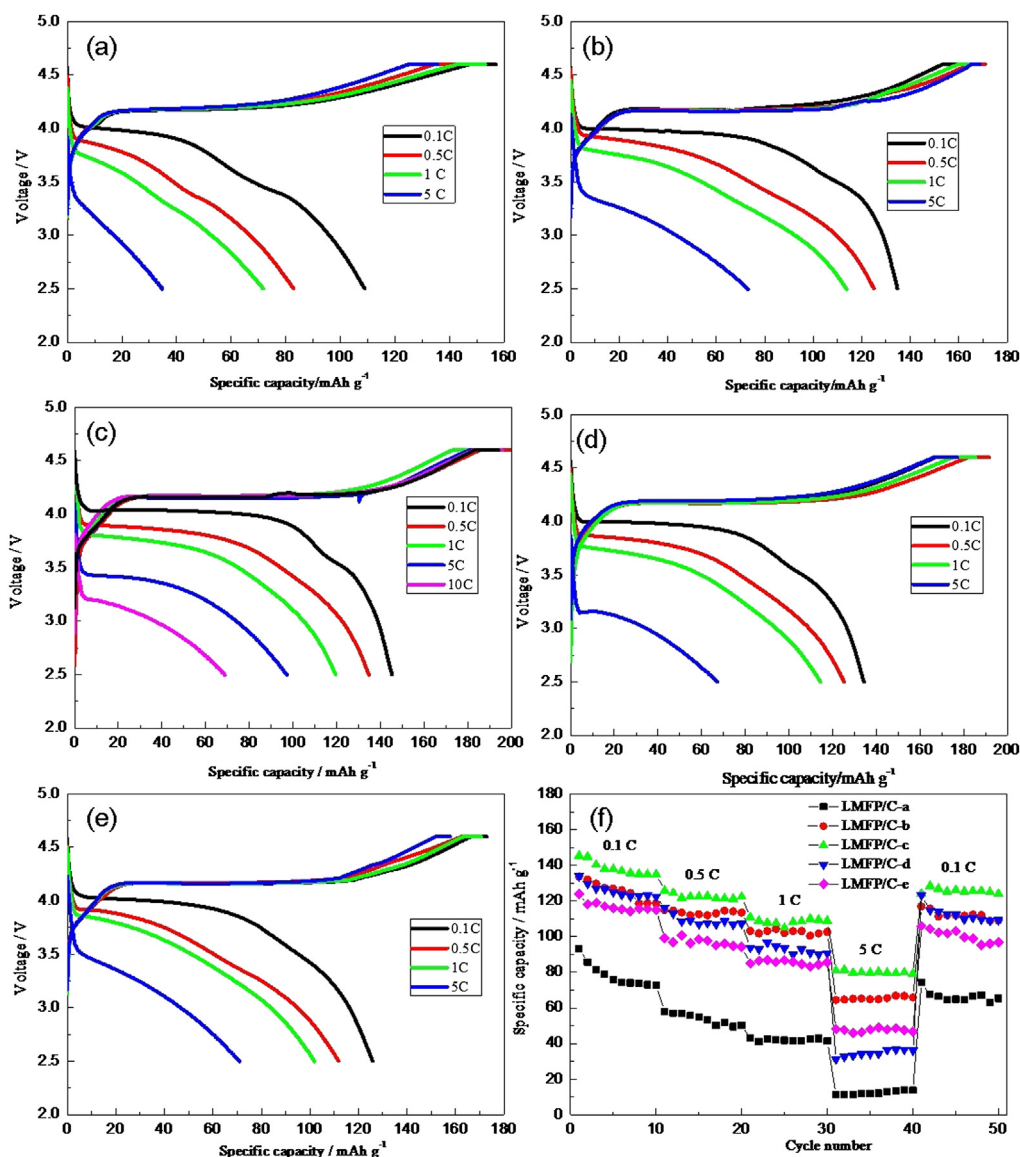


Fig. 8. Initial charge/discharge curves of (a) LMFP/C-a; (b) LMFP/C-b; (c) LMFP/C-c; (d) LMFP/C-d; (e) LMFP/C-e and (f) the rate and cycling performance of the LMFP/C nanoplatelets.

different current rate among these samples. The initial discharge capacities of the LMFP/C-c nanoplatelets are 145 mA h g⁻¹, 134 mA h g⁻¹, 119 mA h g⁻¹, 97 mA h g⁻¹ and 68 mA h g⁻¹ at 0.1 C, 0.5 C, 1 C, 5 C and 10 C, respectively. The excellent electrochemical charge/discharge capability mainly attributes to the shortened pathway for Li⁺ deintercalation/intercalation along the *b* direction. On the other hand, a thin carbon layer on the surface of LMFP nanoplatelets also contributes to the Li⁺ transportation. Fig. 8f exhibits a comparison of the reversible capacities for LMFP/C nanoplatelets over limited cycling at different discharge rates. Although the samples demonstrate good cycling stability at different discharge rates, the capacity decay for these samples with the increasing rate is quite different. Compared with the other four LMFP/C nanoplatelets, the discharge capacity of the LMFP/C-c is greatly increased especially at higher charge–discharge rates. The reversible capacities of LMFP/C-c sample at 0.5 C, 1 C and 5 C rate are about 125 mA h g⁻¹, 110 mA h g⁻¹ and 80 mA h g⁻¹, which are 86%, 75% and 55% of the initial discharge capacity at 0.1 C, respectively. When the charge–discharge rate goes back to 0.1 C after 40 cycles, the reversible capacity can be recovered and maintains at

124 mA h g⁻¹. The excellent electrochemical performance mainly attributes to the smaller length along the *b* direction which is beneficial for enhancing the Li⁺ diffusion capability, and the increase of surface area for the nanosized LMFP/C along (010) plane which is active for Li⁺ intercalation/extraction reaction.

The interfacial properties between electrode and electrolyte were further investigated by electrochemical impedance spectroscopy (EIS). Fig. 9 shows the Nyquist plots of the cells using five LMFP/C electrodes at the fully discharged state after the same cycles. All the EIS profiles exhibit a semicircle in the high frequency region and a straight line in the low frequency region. An intercept at the Z'-axis in high frequency corresponds to the ohmic resistance (*R*_e), which represents the total resistance of the electrolyte, separator, and electrical contacts. A depressed semicircle in the high to intermediate frequency range may be related to the Li⁺ migration resistance through the SEI film formed on the electrode and the charge transfer resistance in both anode and cathode (*R*_{ct}). The inclined line in the lower frequency represents the Warburg impedance, which is associated with the lithium ion diffusion in the LMFP/C particles [43]. From Fig. 9, it can be seen that the *R*_{ct} of

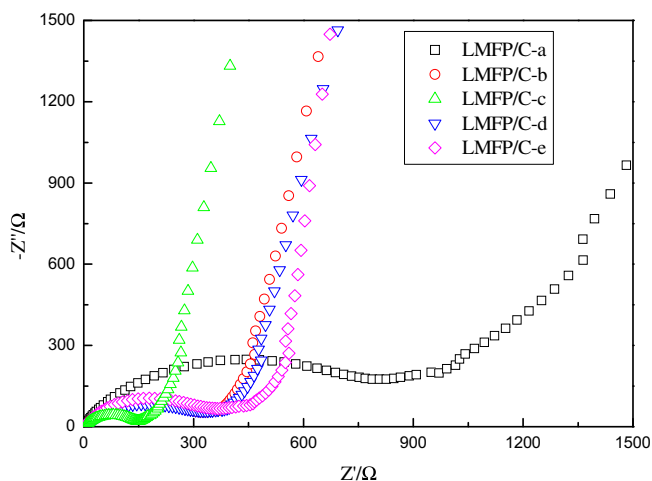


Fig. 9. EIS spectra of the LMFP/C samples.

flakelike LMFP/C-c nanorods (144 Ω) is much smaller than those of the others (larger than 300 Ω), indicating that the smallest size along the *b*-axis have the lowest Li⁺ migration resistance and thus enhance the electrochemical performance.

Fig. 10 shows the relationship between Z'' and square root of frequency ($\omega^{-1/2}$) in the low frequency region. Based on Equation (1), it is found that the Warburg coefficient (σ_w) of LMFP/C nanoplatelets (LMFP/C-c) is $22.43 \Omega \text{ cm}^2 \text{ s}^{-1/2}$.

$$Z' = R_e + R_{ct} + \sigma_w \omega^{-1/2} \quad (1)$$

$$D = R^2 T^2 / 2 A^2 n^4 F^4 C^2 \sigma_w^2 \quad (2)$$

Equation (2) can be used to calculate the Li-ion diffusion coefficient D ($\text{cm}^2 \text{ s}^{-1}$), where R is gas constant ($8.314 \text{ J mol}^{-1} \text{ K}^{-1}$); T is the absolute temperature (K); A is the surface of the cathode (cm^2); n is the number of electrons involved in the redox process (1 in this case); C is the concentration of lithium ion and F is the Faraday constant. The calculated Li-ion diffusion coefficients are shown in Table 2. The results are comparable to the reported data previously [1,2]. It can be found that the LMFP/C nanoplatelets with the smallest size in the *b*-axis have the highest Li-ion diffusion coefficient.

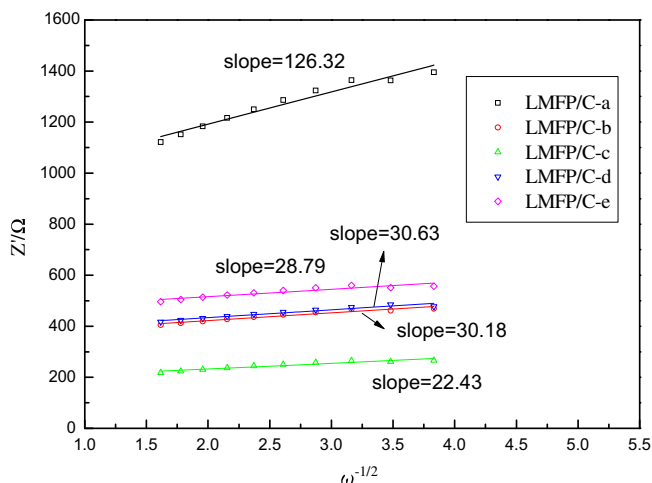


Fig. 10. The relationship between Z'' and $\omega^{-1/2}$ at low frequency.

Table 2

The calculated Li-ion diffusion coefficients of LMFP/C samples.

Samples	σ_w	D ($\text{cm}^2 \text{ s}^{-1}$)
LMFP/C-a	126.32	1.92×10^{-15}
LMFP/C-b	30.18	3.36×10^{-14}
LMFP/C-c	22.43	6.09×10^{-14}
LMFP/C-d	30.63	3.27×10^{-14}
LMFP/C-e	28.79	3.70×10^{-14}

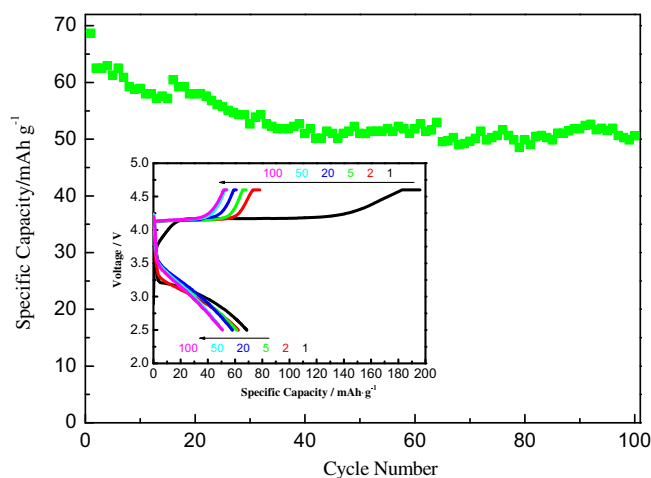


Fig. 11. Cycling performance of the LMFP/C-c sample at 10 C, with a 0.1 C charge rate; charge–discharge profiles of the LMFP-c are also shown as an inset.

It can be deduced that the LMFP/C-c nanoplatelets with the smallest size in the *b*-axis can deliver a high rate performance due to their excellent Li-ion diffusion capability. In order to investigate the rate performance of the flakelike LMFP/C-c nanorods, the coin cell using LMFP/C-c as cathode was discharged at 10 C for 100 cycles. During cycling a low charge rate of 0.1 C was adopted for the comparatively lower polarization during the charging process. The initial specific capacity of LMFP/C-c reaches 68 mA h g^{-1} at 10 C, and can remain 51 mA h g^{-1} after 100 cycles (Fig. 11), and the charge–discharge profiles are also shown as an inset in Fig. 11. The superior performance of LMFP/C could be ascribed to the suitable nanoplatelet-like microstructure with uniform distribution induced by the ascorbic acid addition during the solvothermal synthesis process and the improvement of electrical conductivity due to the carbon coating and Fe doping.

4. Conclusions

In conclusion, by simply adjusting the content of ascorbic acid, LMFP nanoplatelets with controllable *b*-axis thickness as high performance cathode materials for lithium ion batteries have been synthesized successfully via a simple solvothermal process in water–ethanol solvent mixture. Therefore, the ascorbic acid as reducing agent and morphology control agent plays a crucial role in the morphology regulation during the solvothermal process. Such a decreased crystallite size in the *b*-axis direction is of great importance for LMFP due to its intrinsically low conductivity of Li ions and electrons and anisotropic diffusion channels for Li ions. Carbon layer with a thickness of $\sim 3 \text{ nm}$ is coated on the LMFP surface by ball-milling the mixture of LMP and glucose followed by heat treatment. The obtained LMFP/C nanoplatelets with superior electrochemical performance can be a good candidate cathode material for high performance lithium ion batteries.

Acknowledgments

We thank Dr. Jianming Zheng, Dr. Jie Xiao and Prof. Jiguang Zhang of Pacific Northwest National Laboratory (PNNL) for fruitful discussions; This work was partially supported by The Natural Science Foundation of China (no. 50902038), National High Technology Research and Development Program (863 Program) of China (no. 2012AA110203) and Heilong Jiang Postdoctoral Funds for Scientific Research Initiation (no. LBH-Q12084).

References

- [1] A.K. Padhi, K.S. Nanjundaswamy, J.B. Goodenough, *J. Electrochem. Soc.* 144 (1997) 1188.
- [2] L.X. Yuan, Z.H. Wang, W.X. Zhang, X.L. Hu, J.T. Chen, Y.H. Huang, J.B. Goodenough, *Energy Environ. Sci.* 4 (2011) 269.
- [3] Z. Bakenov, I. Taniguchi, *J. Power Sources* 195 (2010) 7445.
- [4] D. Choi, D.H. Wang, I.T. Bae, J. Xiao, Z.M. Nie, W. Wang, V.V. Viswanathan, Y.J. Lee, J.G. Zhang, G.L. Graff, Z.G. Yang, J. Liu, *Nano Lett.* 10 (2010) 2799.
- [5] S.M. Oh, S.W. Oh, C.S. Yoon, B. Scrosati, K. Amine, Y.K. Sun, *Adv. Funct. Mater.* 20 (2010) 3260.
- [6] M. Jo, H.C. Yoo, Y.S. Jung, J. Cho, *J. Power Sources* 216 (2012) 162.
- [7] A.V. Murugan, T. Muraliganth, A. Manthiram, *J. Electrochem. Soc.* 156 (2009) A79.
- [8] K. Saravanan, V. Ramar, P. Balay, J.J. Vittal, *J. Mater. Chem.* 21 (2011) 14925.
- [9] T. Shiratsuchi, S. Okada, T. Doi, J. Yamaki, *Electrochim. Acta* 54 (2009) 3145.
- [10] M. Yonemura, A. Yamada, Y. Takei, N. Sonoyama, R. Kanno, *J. Electrochem. Soc.* 151 (2004) A1352.
- [11] A. Yamada, M. Yonemura, Y. Takei, N. Sonoyama, R. Kanno, *Electrochem. Solid-State Lett.* 8 (2005) A55.
- [12] N. Meethong, H.Y. Huang, S. Speakman, W. Carter, Y.M. Chiang, *Adv. Funct. Mater.* 17 (2007) 1115.
- [13] J.F. Ni, Y. Kawabe, M. Morishita, M. Watada, T. Sakai, *J. Power Sources* 196 (2011) 8104.
- [14] D. Wang, C. Ouyang, T. Drézen, I. Exnar, A. Kay, N.H. Kwon, P. Gouerec, J.H. Miners, M. Wang, M. Grätzel, *J. Electrochem. Soc.* 157 (2010) A225.
- [15] R. Dominko, M. Bele, M. Gaberscek, M. Remskar, D. Hanzel, J.M. Goupil, S. Pejovnik, J. Jamnik, *J. Power Sources* 153 (2006) 274.
- [16] J. Yoshida, M. Stark, J. Holzbock, N. Hüsing, S. Nakanishi, H. Iba, H. Abe, M. Naito, *J. Power Sources* 226 (2013) 122.
- [17] D. Wang, H. Buqa, M. Crouzet, G. Deghenghi, T. Drezen, I. Exnar, N.H. Kwon, J.H. Miners, L. Poletto, M. Gratzel, *J. Power Sources* 189 (2009) 624.
- [18] S. Moon, P. Muralidharan, D.K. Kim, *Ceram. Int.* 38S (2012) S471.
- [19] G. Chen, T.J. Richardson, *J. Power Sources* 195 (2010) 1221.
- [20] Y. Wang, Y. Yang, Y. Yang, H. Shao, *Solid State Commun.* 150 (2010) 81.
- [21] Z.H. Qin, X.F. Zhou, Y.G. Xia, C.L. Tang, Z.P. Liu, *J. Mater. Chem.* 22 (2012) 21144.
- [22] F. Wang, J. Yang, P.F. Gao, Y.N. Nuli, J.L. Wang, *J. Power Sources* 196 (2011) 10258.
- [23] N.H. Kwon, K.M. Fromm, *Electrochim. Acta* 69 (2012) 38.
- [24] C. Delacourt, L. Laffont, R. Bouchet, C. Wurm, J.B. Leriche, M. Morcrette, J.M. Tarascon, C. Masquelier, *J. Electrochem. Soc.* 152 (2005) A913.
- [25] T.H. Kim, H.S. Park, M.H. Lee, S.Y. Lee, H.K. Song, *J. Power Sources* 210 (2012) 1.
- [26] J. Ma, Q.Z. Qin, *J. Power Sources* 148 (2005) 66.
- [27] H. Yang, X.L. Wu, M.H. Cao, Y.G. Guo, *J. Phys. Chem. C* 113 (2009) 3345.
- [28] F. Teng, S. Santhanagopalan, A. Asthana, X. Geng, S.I. Mho, R.S. Yassar, D.D. Meng, *J. Cryst. Growth* 312 (2010) 3493.
- [29] L. Wang, F. Zhou, G. Ceder, *Electrochem. Solid-State Lett.* 11 (2008) A94.
- [30] M.S. Islam, D.J. Driscoll, C.A.J. Fisher, P.R. Slater, *Chem. Mater.* 17 (2005) 5085.
- [31] G.K.P. Dathar, D. Sheppard, K.J. Stevenson, G. Henkelman, *Chem. Mater.* 23 (2011) 4032.
- [32] C.L. Hu, H.H. Yi, H.S. Fang, B. Yang, Y.C. Yao, W.H. Ma, Y.N. Dai, *Electrochem. Commun.* 12 (2010) 1784.
- [33] G.Y. Chen, J.D. Wilcox, T.J. Richardson, *Electrochem. Solid-State Lett.* 11 (2008) A190.
- [34] J. Molenda, W. Ojczyk, K. Swierczek, W. Zajac, F. Krok, J. Dygas, R.S. Liu, *Solid State Ionics* 177 (2006) 2617.
- [35] J. Molenda, W. Ojczyk, J. Marzec, *J. Power Sources* 174 (2007) 689.
- [36] S. Martha, J. Grinblat, O. Haik, E. Zinigrad, T. Drezen, J. Miners, I. Exnar, A. Kay, B. Markovsky, D. Aurbach, *Angew. Chem.* 121 (2009) 8711.
- [37] B. Zhang, X.J. Wang, H. Li, X.J. Huang, *J. Power Sources* 196 (2011) 6992.
- [38] S.M. Oh, H.G. Jung, C.S. Yoon, S.T. Myung, Z.H. Chen, K. Amine, Y.K. Sun, *J. Power Sources* 196 (2011) 6924.
- [39] Y.Z. Dong, L. Wang, S.L. Zhang, Y.M. Zhao, J.P. Zhou, H. Xie, J.B. Goodenough, *J. Power Sources* 215 (2012) 116.
- [40] R.D. Shannon, *Acta Crystallogr. Sect. A* 32 (1976) 751.
- [41] Y.J. Zhong, J.T. Li, Z.G. Wu, X.D. Guo, B.H. Zhong, S.G. Sun, *J. Power Sources* 234 (2013) 217.
- [42] P.R. Kumar, M. Venkateswarlu, M. Misra, A.K. Mohanty, N. Satyanarayana, *J. Electrochem. Soc.* 158 (2011) A227.
- [43] T.N.L. Doan, Z. Bakenov, I. Taniguchi, *Adv. Powder Technol.* 21 (2010) 187.